




Article

Vacuum and Low-Temperature Characteristics of Silicon Oxynitride-Based Bipolar RRAM

Nayan C. Das ¹, Minjae Kim ¹, Sung-Min Hong ¹ and Jae-Hyung Jang ^{2,*}

¹ Gwangju Institute of Science and Technology, School of Electrical Engineering and Computer Science, Gwangju 61005, Korea; nayan@gm.gist.ac.kr (N.C.D.); min7kim9@gm.gist.ac.kr (M.K.); smhong@gist.ac.kr (S.-M.H.)

² Korea Institute of Energy Technology, School of Energy Technology, Naju 58330, Korea

* Correspondence: jjang@kentech.ac.kr; Tel.: +82-61-330-9650

Abstract: This study investigates the switching characteristics of the silicon oxynitride (SiO_xN_y)-based bipolar resistive random-access memory (RRAM) devices at different operating ambiances at temperatures ranging from 300 K to 77 K. The operating ambiances (open air or vacuum) and temperature affect the device's performance. The electroforming-free multilevel bipolar Au/Ni/ SiO_xN_y /p⁺-Si RRAM device (in open-air) becomes bilevel in a vacuum with an on/off ratio $>10^4$ and promising data retention properties. The device becomes more resistive with cryogenic temperatures. The experimental results indicate that the presence and absence of moisture (hydrogen and hydroxyl groups) in open air and vacuum, respectively, alter the elemental composition of the amorphous SiO_xN_y active layer and Ni/ SiO_xN_y interface region. Consequently, this affects the overall device performance. Filament-type resistive switching and trap-controlled space charge limited conduction (SCLC) mechanisms in the bulk SiO_xN_y layer are confirmed.

Keywords: bipolar; cryogenic temperature; operating ambiances; RRAM



Citation: Das, N.C.; Kim, M.; Hong, S.-M.; Jang, J.-H. Vacuum and Low-Temperature Characteristics of Silicon Oxynitride-Based Bipolar RRAM. *Micromachines* **2022**, *13*, 604. <https://doi.org/10.3390/mi13040604>

Academic Editor: Peng Huang

Received: 15 March 2022

Accepted: 11 April 2022

Published: 12 April 2022

Publisher's Note: MDPI stays neutral with regard to jurisdictional claims in published maps and institutional affiliations.



Copyright: © 2022 by the authors. Licensee MDPI, Basel, Switzerland. This article is an open access article distributed under the terms and conditions of the Creative Commons Attribution (CC BY) license (<https://creativecommons.org/licenses/by/4.0/>).

1. Introduction

Low-temperature electronics technology has the potential to improve device and circuit performances. When semiconductor devices are operated at a cryogenic temperature (approximately 123 K and below), the system performance can be improved [1]. Moreover, recent research interest in quantum computing, space electronics, and superconducting circuits has also led to developments in cryogenic data storage technology [2,3]. However, one of the significant challenges to implementing cryogenic electronics is finding a suitable and compatible cryogenic memory that can operate at cryogenic temperatures [2–5].

Resistance-based (non-superconducting) memories offer better scalability, faster speed, and lower power consumption than charge-based memories among different cryogenic memory technologies. Moreover, resistance-based memories provide nonvolatility. Among the resistance-based memories, resistive random access memory (RRAM) devices are strong candidates for a cryogenic memory due to their low-power operation, excellent scalability, high reliability, and simple manufacturing processes [2–7].

Although extensive studies have been conducted on RRAM devices, most studies were completed in open air at room temperature. Few studies investigated the effects of air, oxygen, and nitrogen partial pressure on RRAM device performance by varying operating ambiance [6,8,9]. Studies also showed that the electroforming process is not possible in a vacuum for SiO_2 -, Ta_2O_5 -, and HfO_2 -based devices [10–14]. Only two binary oxide material (HfO_x and Cu-doped silica)-based RRAM devices have been studied at cryogenic temperatures to date [4,5,15–19]. All other studies (except for Shang et al. [18]) required an electroforming process to activate the resistive switching properties in open air at room temperature before measuring device performance cryogenic temperatures [4,5,15–19]. Even

though cryogenic temperature memory devices ideally require temperature-independent properties, this has not yet been explored [20].

In order to overcome the limitations mentioned above, a reliable RRAM device, which works in a vacuum at cryogenic temperatures, is needed. Thus, it is essential to study in detail the interaction of the RRAM device with the ambience (open air and vacuum), when varying the temperature from room temperature to cryogenic temperatures. After developing a multilevel bipolar electroforming-free resistive switching memory (Au/Ni/SiO_xN_y/p⁺-Si device) in open air at room temperature [21], the next obvious step is to explore the feasibility of the device in a vacuum and at cryogenic temperatures.

This work reports that Au/Ni/SiO_xN_y/p⁺-Si RRAM devices are operable at cryogenic temperatures without pretreatment. They exhibit favorable resistive switching properties in the ambience at room temperature and at temperatures ranging from 77 K to 300 K. The change in operating ambience influences the performance of the devices. Depending on the operating environment, the availability of the weakly bonded hydroxyl groups influences the surface chemistry of the amorphous SiO_xN_y active layer and the Ni/SiO_xN_y interface, which subsequently changes the elemental composition of the Ni/SiO_xN_y interface region and affects the device performance.

2. Materials and Methods

The 10 nm thick SiO_xN_y thin films were deposited by plasma-enhanced chemical vapor deposition (PECVD) on a p⁺-Si substrate (boron-doped, 3.0 mΩ·cm) at 300 °C. The gas mixture, N₂O/SiH₄/NH₃/N₂ (60/400/20/600 SCCM), was supplied under a working pressure of 650 mTorr and an RF power of 15 W (30.6 W/mm²). A circular-shaped Au/Ni (150/40 nm) top electrode with a radius of 50 μm was deposited by e-beam evaporation through a shadow mask to complete the device fabrication. The heavily doped p⁺-Si substrate served as the bottom electrode. For X-ray photoelectron spectroscopy (XPS; NEXSA, Fisher Scientific, 168 Third Avenue, Waltham, MA, USA) and Fourier-transform infrared (FTIR) absorbance spectroscopy measurement, 50 nm and 1 μm thick SiO_xN_y films were grown separately. The IR spectra of SiO_xN_y films under vacuum and ambient conditions were measured by a Vertex 80v IR spectrometer equipped with an infrared reflection absorbance (IRRAS) accessory (Bruker A513, incident angle 45°, Bruker Optics, Ettlingen, Germany) and MCT detector. The pressure in the vacuum was about 1.27 hPa (9.5 × 10⁻¹ torr).

The electrical characteristics of the memory devices were measured using a semiconductor parameter analyzer (HP-4155A; Hewlett-Packard Company, 3000 Hanover Street, Palo Alto, CA, USA). The electrical characteristics of RRAM devices in a vacuum environment and at cryogenic temperatures were measured using an MS-TECH Vacuum Chamber Probe Station (<10⁻⁵ torr). A voltage was applied directly to the top electrode, while the bottom electrode was grounded.

Three different batches of samples for each sample type were analyzed to confirm the reproducibility. A batch consisted of more than 20 devices, and more than 50 devices were measured in each condition (in a vacuum at 300 K to 77 K) to confirm the observations and conclusions. Due to the few process variables involved in the device fabrications and considering that each process condition was well controlled, the performance of different devices in the same batch and different batches was almost the same. Additionally, all devices showed similar cycle-to-cycle variations. The range of device-to-device variation was smaller than that of cycle-to-cycle variation.

3. Results and Discussion

3.1. Properties of SiO_xN_y Film

Compositional analysis of the PECVD grown amorphous SiO_xN_y film is shown in Figure 1. The XPS depth profile analysis shows that the Si/N/O atomic percentage (45.52%, 28.91%, and 25.58%) and ratio (1:0.64:0.56) of the as-deposited SiO_xN_y film were constant

throughout the film, indicating a sufficient number of oxygen vacancies and nitride-related traps in the layer (Figure 1a).

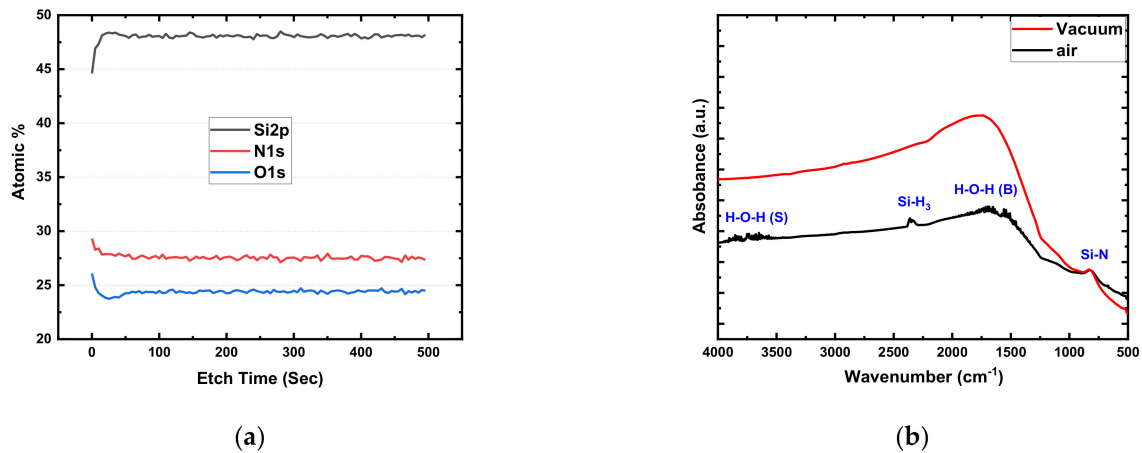


Figure 1. Compositional analysis of SiO_xN_y thin film: (a) XPS depth profile with atomic percentages; (b) FTIR absorbance spectra measured in open-air and vacuum environments.

FTIR absorbance spectra for the SiO_xN_y film measured in open-air and vacuum environments are shown in Figure 1b. The stable characteristic absorbance peak of the Si–N bond was found at 831 cm⁻¹ for both measurement conditions. However, many weak absorption peaks were observed in the ranges 3800–3500 cm⁻¹ and 1700–1450 cm⁻¹, associated with the weak binding between Si²⁺ sites and different vibrational modes (stretching and bending) of hydroxyl groups in open-air measurement conditions [22–26].

In SiO_xN_y, the Si–OH bond vibrations typically peaked at around 3500 cm⁻¹, and the band of N–H bonds peaked at about 3320 cm⁻¹. The absorption band in the range of 2300–2390 cm⁻¹ was due to the Si–H stretching vibrations [26]. Si–H₃ vibration resulted in an absorption band around 2255 cm⁻¹, and this band could shift further to a higher wavenumber if more nitrogen atoms are introduced into the thin film [26]. These hydroxyl groups indicated the presence of H₂O on the surface of the amorphous SiO_xN_y that was absorbed from the ambience during the fabrication process. In a vacuum environment, all weakly bonded hydrogen and hydroxyl groups are easily removed from the surface of the amorphous SiO_xN_y thin film [27–29].

3.2. Electrical Characteristics of Au/Ni/SiO_xN_y/p⁺-Si Device

The viability of the Au/Ni/SiO_xN_y/p⁺-Si memory device at cryogenic temperature was investigated in two steps. At first, the device performances were measured in a vacuum chamber and at room temperature. After that, the device performance was measured in a vacuum chamber at 77 K.

3.2.1. Device Performance in a Vacuum at Room Temperature

In the open-air environment, the current–voltage (I–V) measurement of the Au/Ni/SiO_xN_y/p⁺-Si devices with a 50 μm radius was conducted by applying double-sweep DC voltage in the sequence of 0 V → +7 V → 0 V → –7 V → 0 V with a 0.25 mA compliance current (I_{cc}) and a 50 mV step. The electroforming-free bipolar multilevel switching operation of the 10 nm thick SiO_xN_y-based device (black) is shown in Figure 2a. The stability of the intermediate resistance state (IRS) was confirmed by cycling 0 V → +6.5 V → 0 V → –7 V → 0 V, which is shown in green (Figure 2a). A detailed study of the multilevel electroforming-free bipolar resistive switching behavior of the devices was reported separately [21].

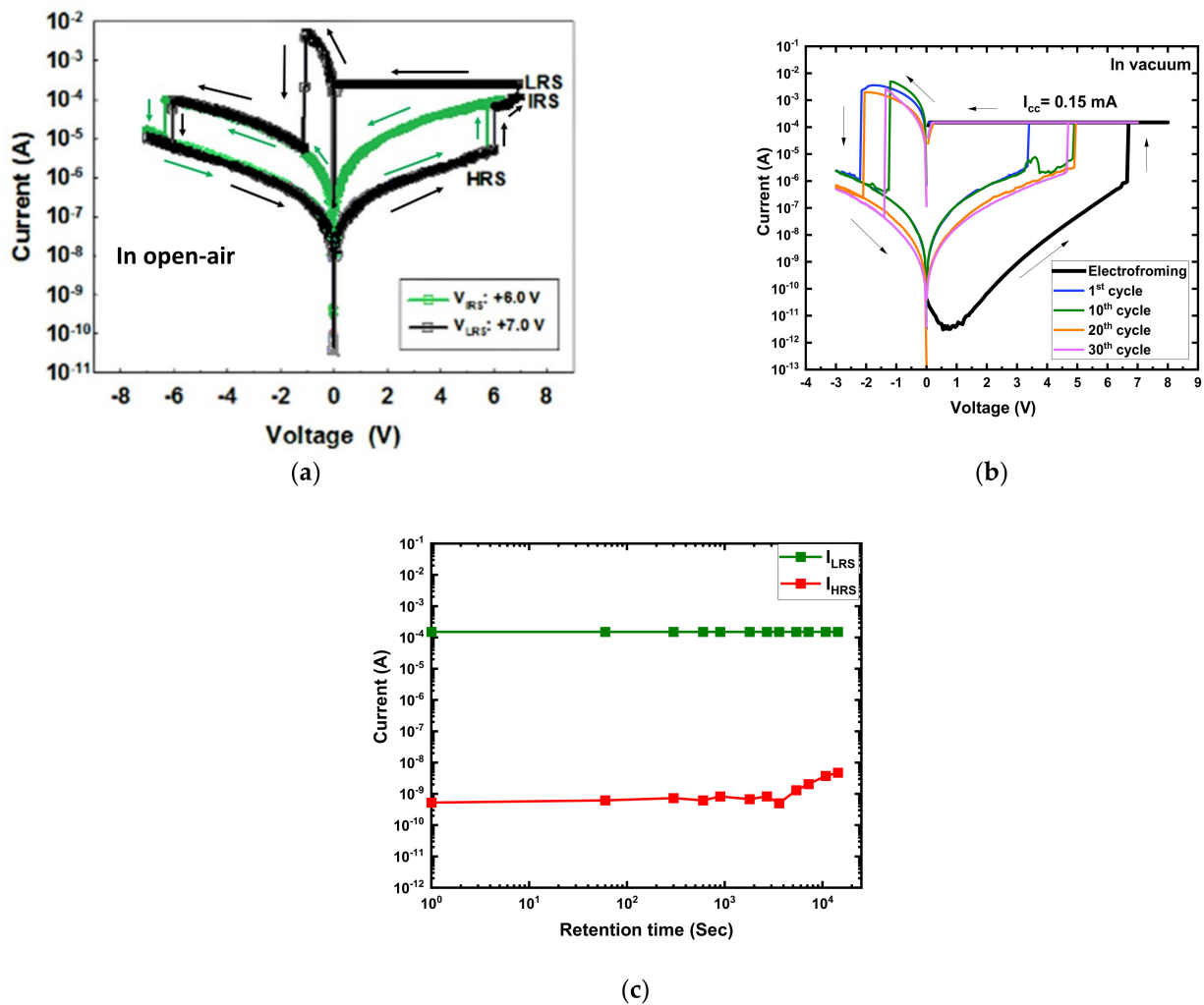


Figure 2. Typical I–V characteristics of Au/Ni/SiO_xN_y/p⁺-Si at room temperature (a) in open air [21], and (b) in a vacuum; (c) data retention characteristics of the device in a vacuum at 300 K.

I–V measurement of the devices was carried out when the chamber was in a vacuum ($<10^{-3}$ torr) at 300 K to investigate the effects of the operating environment on the device performance. Figure 2b shows the I–V characteristics of the device in a vacuum at 300 K. In the vacuum environment, basic operating parameters such as the 0.15 mA I_{cc} and 50 mV step were kept constant. The first double-sweep DC voltage in the $0\text{ V} \rightarrow +8\text{ V} \rightarrow 0\text{ V} \rightarrow -3\text{ V} \rightarrow 0\text{ V}$ was applied for the electroforming process. When the positive bias voltage was applied, the current increased sharply at the electroforming voltage (V_{FORM}) around +7 V, and the device reached the low resistance state (LRS). The device returned to the new high resistance state (HRS) when a negative voltage was applied. After electroforming, the sequence was changed to $0\text{ V} \rightarrow +7\text{ V} \rightarrow 0\text{ V} \rightarrow -3\text{ V} \rightarrow 0\text{ V}$ (Figure 2b). The SET process occurred in the range of +3.2 to +5.0 V (V_{SET}), and the RESET process occurred at the RESET voltage (V_{RESET}) in the range of -1.30 to -2.15 V. The LRS current (I_{LRS}) and HRS current (I_{HRS}) values of the device were read at -0.50 V (V_{READ}). The data retention characteristics of the device in a vacuum at 300 K are shown in Figure 3c. The device exhibited promising data retention over 10^4 s with an on/off ratio higher than 10^4 .

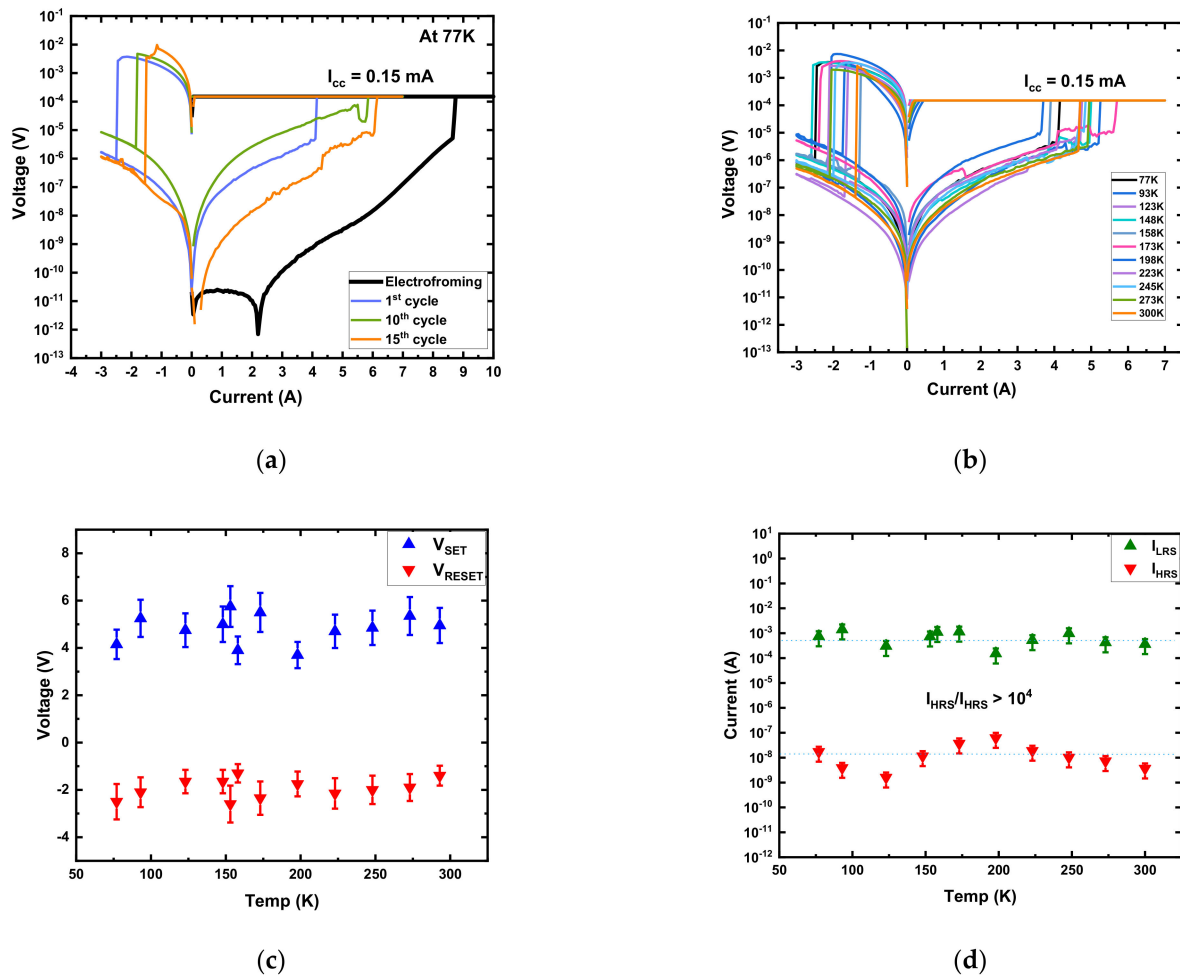


Figure 3. Au/Ni/SiO_xN_y/p⁺-Si memory device performance in a vacuum. (a) Typical I–V curves at 77 K; (b) typical I–V curves with temperature variation from 77 K to 300 K; (c) V_{SET} and V_{RESET} vs. temperature; (d) I_{LRS} and I_{HRS} vs. temperature.

The multilevel Au/Ni/SiO_xN_y/p⁺-Si RRAM device became bilevel with an on/off ratio >10⁴ when the operating ambience was changed from open air to vacuum. The device also exhibited three-order-higher initial resistance (~GΩ) in a vacuum at room temperature than the device (~MΩ) measured in the open-air environment. The pristine device requires an electroforming process to activate resistive switching properties in a vacuum where the device operates electroforming-free in open air at 300 K. The electroforming-free characteristic of the device in open air is caused by the combined effects of sufficient internal defects (oxygen vacancies and nitride-related traps) and the presence of external defects (O–H, and –H groups) on the surface of the amorphous SiO_xN_y active layer. The O–H groups provide additional charges and facilitate the formation of anion vacancies at the interface of the Ni/SiO_xN_y [11,14,30–32]. In a vacuum, weakly bonded hydrogen and hydroxyl groups are removed from the surface of the amorphous SiO_xN_y thin film, which makes the active layer more resistive; the overall initial resistance of the device increases by a factor of three, and the IRS disappears [10–14].

The effects of the device size (area) and the active layer thickness on the device performance were explained in detail in a previous study [21]. The I_{LRS} independence of the area implies that the current conduction was dominated by filamentary conduction [21,33]. The V_{SET} and V_{RESET} active layer thickness dependencies show that filament-type resistive switching was bulk-dependent, indicating that a conductive filament (CF) was formed from the bottom electrode to the top electrode through the bulk SiO_xN_y layer [21,33].

After electroforming, the CF dissolved partially at its weak point during the RESET process, and the device reached a new HRS, which was less resistive than the initial HRS. Further SET/RESET processes happened through reconstruction and partial breakdown of the CF, requiring a smaller magnitude of voltages ($|V_{\text{SET}}|$ and $|V_{\text{RESET}}|$) than the $|V_{\text{FORM}}|$ [34].

3.2.2. Device Performance in a Vacuum at Cryogenic Temperature

The resistive switching performance of the Au/Ni/SiO_xN_y/p⁺-Si memory devices in a vacuum ($<10^{-5}$ torr) at 77 K is shown in Figure 3a. For the first sweep, DC voltage was applied in the sequence of 0 V → +10 V → 0 V → −3 V → 0 V. The pristine device was in the HRS with a resistance of 100 GΩ at a low temperature, which is much higher than the resistance (~10 GΩ) in vacuum at room temperature. V_{FORM} (≈+8.5 V) was also higher than in vacuum at 300 K (≈+7 V). The cryogenic temperature made the device more resistive due to the semiconducting behavior, indicating the possible involvement of the thermionic conduction process. The formation and dissolution of a CF include charge transfer, ion motion, and nucleation, which are affected by the change in temperature [4]. With the reduction in temperature to 77 K, the thermal energies of oxygen vacancies and ions are also reduced. Consequently, the device needs a higher V_{FORM} to form CFs [5,17]. As a result, increases in the initial resistance and V_{FORM} were observed at low temperatures.

During the electroforming process in vacuum, both at 300 K and at 77 K, there was an abnormal dip in the current at a positive bias side, as shown in the black in Figures 2b and 3a. The abnormal dips were attributed to the negative differential resistance (NDR) effect. In general, a higher bias voltage corresponds to a larger current. However, the phenomenon when the current decreases with the increase in bias voltage is called NDR, which has been observed during the electroforming or set process [35–39]. The NDR phenomena are mainly observed in RRAM devices due to the trap/de-trap of electronic carriers between deeply localized states induced by implanted metal nanoparticles [36,37] or the accumulation of defects caused by junction reinstatement [35]. They can also be observed due to the recombination between oxygen vacancies and the thermally released oxygen ions from the oxide interface layer [38,39]. In the Au/Ni/SiO_xN_y/p⁺-Si device, the NDR phenomena were mainly observed during the electroforming process due to the trapping of electronic carriers in the deeply localized states induced by oxygen vacancies and nitride-related traps in the fresh device.

After electroforming, the cycle sequence was 0 V → +7 V → 0 V → −3 V → 0 V. V_{SET} , V_{RESET} , I_{LRS} , and I_{HRS} followed a similar pattern to that in vacuum at room temperature (Figure 3a). The device performed well with a minimum on/off ratio $>10^4$ at 77 K.

At 77 K, the variability in the I–V curves of the device performance resulted from different CF configurations of oxygen vacancies and nitride-related traps between the Ni and p⁺-Si with varying heights of the barrier due to the different bias cycles [5]. At 77 K, the LRS also showed more uniformity than HRS.

The I–V characteristics were measured from 77 K to 300 K after electroforming at 77 K to investigate the effect of the temperature variation on the device's performance (Figure 3b). Voltages (V_{SET} and V_{RESET}) and currents (I_{LRS} and I_{HRS}) as a function of temperatures are presented in Figure 3c,d, respectively.

As demonstrated in Figure 3c,d, after electroforming, the random variation in V_{SET} , V_{RESET} , I_{LRS} , and I_{HRS} implies that the resistive switching characteristics were less affected by temperature variation than cycle-to-cycle variation. The variation in V_{RESET} and V_{SET} indicates that the CFs were partially ruptured after RESET [4,40]. The partially ruptured CF in the RESET process was attributed to the combined effects of the oxygen vacancy recombination with nitride-related traps by electric fields (primarily) and localized Joule heating (assisting) [19,33,41,42]. Joule heating can subdue the operating ambient temperature effect as the local temperature due to Joule heating can surpass the ambient temperature by a significant amount [20,42,43]. As a result, after electroforming, V_{SET} , V_{RESET} , I_{LRS} , and I_{HRS} of the device were less affected by the temperature variation, providing these potential

devices with stability in the cryogenic temperature range, appropriate for applications using RRAM technology [44].

3.2.3. Conduction and Switching Mechanism in Vacuum at 77 K

A typical I–V curve from Figure 3a was replotted as $\log(I)$ – $\log(V)$ with curve fittings to explore the current conduction process of the Au/Ni/SiO_xN_y/p⁺-Si device at 77 K after electroforming in Figure 4. The HRS and LRS of the negative voltage regions were divided into S1, S2, S3, S4, and S5 (Figure 4a). Similarly, the positive voltage regions were divided into SP1, SP2, SP3, SP4, and SP5 (Figure 4b).

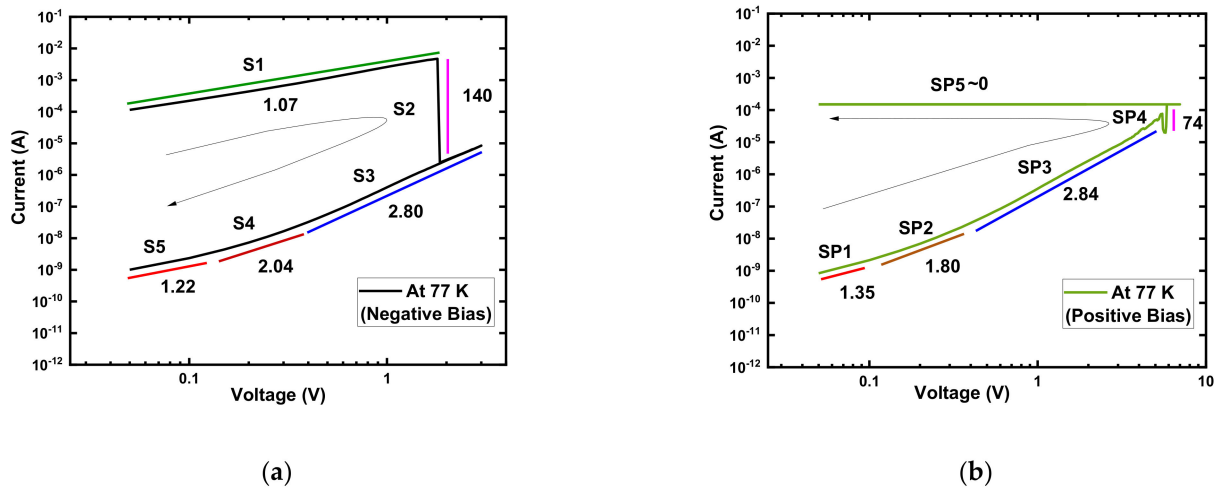


Figure 4. Log I –log V characteristics of Au/Ni/SiO_xN_y/p⁺-Si memory devices with $I_{cc} = 0.15$ mA at 77 K. (a) Negative bias voltage region; (b) positive bias voltage region with slopes of different parts.

In the negative voltage region, the slope of the LRS (S1: 1.07) indicated ohmic conduction ($I \propto V$). At the RESET voltage region (S2: 140), the conduction mechanism followed Child's law ($I \propto V^n$ where $n = 4$ –150). At higher voltages, the slopes of the HRS (S3: 2.8, S4: 2.04) followed Child's law ($I \propto V^n$ where $n = 1.5$ –3). The positive voltage region also showed a similar pattern even though the I_{cc} limit controlled the LRS current. In the negative and positive low-voltage regions, the slopes (S5: 1.22, SP1: 1.35) were slightly higher than 1, which can be attributed to the incomplete rupture and formation of the CF during the RESET and SET processes after electroforming at low temperatures.

The above analysis and an earlier study [21] showed that the conduction mechanism for the device is always the trap-controlled SCLC regardless of operating environment and temperature [21,45–48].

According to the current conduction mechanism analysis, the resistive switching mechanism with the schematics of the Au/Ni/SiO_xN_y/p⁺-Si memory device in cryogenic temperature is proposed below (Figure 5).

In an open-air environment, the as-prepared device contained a sufficient number of internal defects and external defects. The internal defects were a combination of silicon dangling bonds, oxygen vacancies, and nitride-related traps in the bulk of the initial SiO_xN_y layer [49] (Figure 5a). These silicon dangling bonds and oxygen vacancies play major roles in resistive switching [21,25,50]. The external defects were the weakly bonded O–H groups on the surface of SiO_xN_y, facilitating the creation of anion vacancies at the interface by disassociating into differently charged species (O^{2-} and H^+). Thus, the presence of the ionic charge carriers at the interface region was altered from the bulk SiO_xN_y and increased the interface region's conductivity [11,14,30,31]. All defects (internal and external) in the devices were considered as traps (Figure 5a). The external defects (hydrogen and hydroxyl groups) were removed from the Ni/SiO_xN_y interface in vacuum. At 77 K, the pristine device became more resistive due to the reduction in thermal energies of ions

and oxygen vacancies [5,17] (Figure 5b). The switching mechanism was fundamentally related to the oxygen and nitrogen content in the SiO_xN_y layer. When the positive voltage increased beyond the V_{FORM} , CFs of oxygen vacancies were formed between the Ni and p^+ -Si through the bulk SiO_xN_y layer in the electroforming process (not explicitly shown in Figure 5), and the device resistance state changed from HRS to LRS. The Ni layer acted as a charge reservoir, and oxygen ions traveled by hopping through the nitride-related traps of the SiO_xN_y layer under the applied positive voltage. After the initial formation of a CF, electronic carriers hopped through the oxygen vacancy and nitride-related trap-based CFs at V_{SET} (Figure 5c). When the negative bias voltage approached V_{RESET} , the oxygen ions traveled back from the Ni layer and recombined with the oxygen vacancies. This capture process broke the oxygen vacancy-based CFs, leading to resistive switching from the LRS to HRS (Figure 5d) [21].

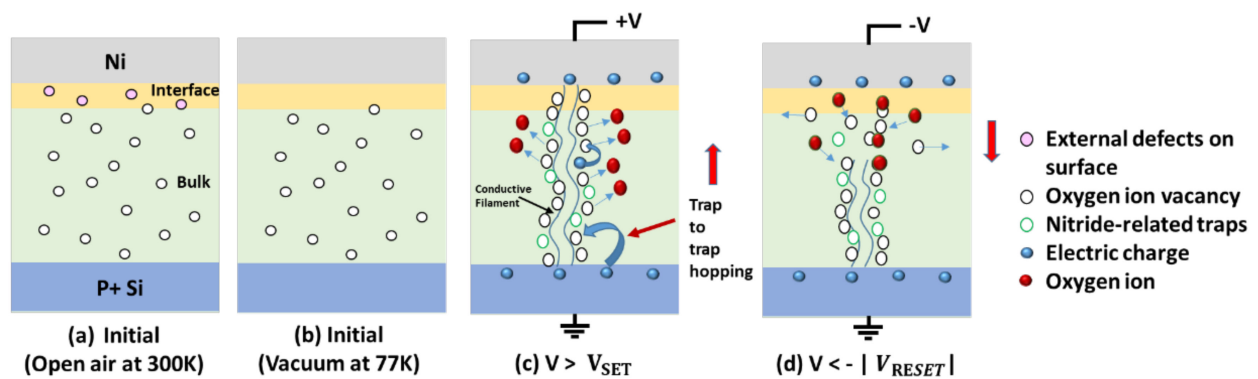


Figure 5. Schematics of proposed switching mechanism of Au/Ni/SiO_xN_y/p⁺-Si memory device in a vacuum at 77 K.

4. Conclusions

Fully functional Au/Ni/SiO_xN_y/p⁺-Si memory devices were successfully fabricated, which could operate in open-air and vacuum environments at temperatures ranging from 300 K to 77 K. In an open-air laboratory environment, the device showed electroforming-free multilevel bipolar resistive switching. However, the multilevel RRAM device became bilevel in a vacuum with an on/off ratio >10⁴ at room temperature. The device showed promising stability with data retention higher than 10⁴ s. At 77 K, the device became more resistive than at room temperature, but a high on/off ratio (>10⁴) was maintained. The presence (in the atmospheric environment) and absence (in vacuum) of moisture (hydrogen and hydroxyl groups)-related defects at the amorphous SiO_xN_y active layer and the Ni/SiO_xN_y interface were determined by the operating environment. These hydrogen and hydroxyl groups subsequently changed the Ni/SiO_xN_y interface region's elemental compositions and affected the device performance.

Author Contributions: Conceptualization, N.C.D.; validation, M.K.; writing—original draft preparation, N.C.D.; writing—review and editing, N.C.D., S.-M.H. and J.-H.J.; supervision, S.-M.H. and J.-H.J. All authors have read and agreed to the published version of the manuscript.

Funding: This work was supported in part by the Creative Materials Discovery Program through the National Research Foundation of Korea (NRF) funded by the Ministry of Science and ICT (NRF-2017M3D1A1040828) and Samsung Electronics.

Acknowledgments: The IR spectra were measured at the Kangwon Radiation Convergence Research Support Center of Korea Basic Science Institute (KBSI), Kangwon National University.

Conflicts of Interest: The authors declare no conflict of interest.

References

1. Foty, D. Symposium on Low Temperature Electronic Device Operation. In Proceedings of the 1991 Spring Meeting of The Electrochemical Society, Washington, DC, USA, 7–9 May 1991; Electrochemical Society: Pennington, NJ, USA, 1991.
2. Alam, S.; Hossain, S.; Srinivasa, S.R.; Aziz, A. Cryogenic Memory Technologies. Available online: <https://arxiv.org/abs/2111.09436> (accessed on 2 March 2022).
3. Cryogenic Memory-Rambus. Available online: <https://www.rambus.com/emerging-solutions/cryogenic-memory/> (accessed on 3 May 2021).
4. Chen, W.; Chamele, N.; Barnaby, H.J.; Kozicki, M.N. Low-Temperature Characterization of Cu–Cu: Silica-Based Programmable. *IEEE Electron Device Lett.* **2017**, *38*, 1244–1247. [[CrossRef](#)]
5. Fang, R.; Chen, W.; Gao, L.; Yu, W.; Yu, S. Low-Temperature Characteristics of HfO_x-Based Resistive Random Access Memory. *IEEE Electron Device Lett.* **2015**, *36*, 567–569. [[CrossRef](#)]
6. Nagashima, K.; Yanagida, T.; Oka, K.; Kanai, M.; Klamchuen, A.; Rahong, S.; Meng, G.; Horprathum, M.; Xu, B.; Zhuge, F.; et al. Prominent thermodynamical interaction with surroundings on nanoscale memristive switching of metal oxides. *Nano Lett.* **2012**, *12*, 5684–5690. [[CrossRef](#)] [[PubMed](#)]
7. Das, N.C.; Kim, M.; Rani, J.R.; Hong, S.-M.; Jang, J.-H. Electroforming-Free Bipolar Resistive Switching Memory Based on Magnesium Fluoride. *Micromachines* **2021**, *12*, 1049. [[CrossRef](#)]
8. Goux, L.; Czarnecki, P.; Chen, Y.Y.; Pantisano, L.; Wang, X.P.; Degraeve, R.; Govoreanu, B.; Jurczak, M.; Wouters, D.J.; Altimime, L. Evidences of oxygen-mediated resistive-switching mechanism in TiN/HfO₂/Pt cells. *Appl. Phys. Lett.* **2010**, *97*, 243509. [[CrossRef](#)]
9. Chen, K.H.; Tsai, T.M.; Cheng, C.M.; Huang, S.J.; Chang, K.C.; Liang, S.P.; Young, T.F. Schottky emission distance and barrier height properties of bipolar switching Gd:SiO_x RRAM devices under different oxygen concentration environments. *Materials* **2017**, *11*, 43. [[CrossRef](#)]
10. Tsuruoka, T.; Terabe, K.; Hasegawa, T.; Valov, I.; Waser, R.; Aono, M. Effects of moisture on the switching characteristics of oxide-based, gapless-type atomic switches. *Adv. Funct. Mater.* **2012**, *22*, 70–77. [[CrossRef](#)]
11. Valov, I.; Tsuruoka, T. Effects of moisture and redox reactions in VCM and ECM resistive switching memories. *J. Phys. D Appl. Phys.* **2018**, *51*, 413001. [[CrossRef](#)]
12. Tappertzhofen, S.; Hempel, M.; Valov, I.; Waser, R. Proton mobility in SiO₂ thin films and impact of hydrogen and humidity on the resistive switching effect. *Mater. Res. Soc. Symp. Proc.* **2011**, *1330*, 1–6. [[CrossRef](#)]
13. Tappertzhofen, S.; Valov, I.; Tsuruoka, T.; Hasegawa, T.; Waser, R.; Aono, M. Generic relevance of counter charges for cation-based nanoscale resistive switching memories. *ACS Nano* **2013**, *7*, 6396–6402. [[CrossRef](#)]
14. Lübben, M.; Wiefels, S.; Waser, R.; Valov, I. Processes and Effects of Oxygen and Moisture in Resistively Switching TaO_x and HfO_x. *Adv. Electron Mater.* **2018**, *4*, 1700458. [[CrossRef](#)]
15. Wang, M.; Bi, C.; Li, L.; Long, S.; Liu, Q.; Lv, H.; Lu, N.; Sun, P.; Liu, M. Thermoelectric seebeck effect in oxide-based resistive switching memory. *Nat. Commun.* **2014**, *5*, 4598. [[CrossRef](#)] [[PubMed](#)]
16. Walczyk, C.; Walczyk, D.; Schroeder, T.; Bertaud, T.; Sowińska, M.; Lukosius, M.; Fraschke, M.; Wolansky, D.; Tillack, B.; Miranda, E.; et al. Impact of temperature on the resistive switching behavior of embedded HfO₂-based RRAM devices. *IEEE Trans. Electron Devices* **2011**, *58*, 3124–3131. [[CrossRef](#)]
17. Ahn, C.; Kim, S.; Gokmen, T.; Dial, O.; Ritter, M.; Wong, H.S.P. Temperature-dependent studies of the electrical properties and the conduction mechanism of HfO_x-based RRAM. In Proceedings of the Technical Program—2014 International Symposium on VLSI Technology, Systems and Application (VLSI-TSA), Hsinchu, Taiwan, 28–30 April 2014; pp. 1–2. [[CrossRef](#)]
18. Shang, J.; Liu, G.; Yang, H.; Zhu, X.; Chen, X.; Tan, H.; Hu, B.; Pan, L.; Xue, W.; Li, R.W. Thermally stable transparent resistive random access memory based on all-oxide heterostructures. *Adv. Funct. Mater.* **2014**, *24*, 2171–2179. [[CrossRef](#)]
19. Zhou, P.; Ye, L.; Sun, Q.Q.; Chen, L.; Ding, S.J.; Jiang, A.Q.; Zhang, D.W. The temperature dependence in nanoresistive switching of HfAlO. *IEEE Trans. Nanotechnol.* **2012**, *11*, 1059–1062. [[CrossRef](#)]
20. Das, N.C.; Kim, M.; Rani, J.R.; Hong, S. Low-temperature characteristics of magnesium fluoride based bipolar RRAM devices. *Nanoscale* **2022**, *14*, 3738–3747. [[CrossRef](#)]
21. Das, N.C.; Oh, S.I.; Rani, J.R.; Hong, S.M.; Jang, J.H. Multilevel bipolar electroforming-free resistive switching memory based on silicon oxynitride. *Appl. Sci.* **2020**, *10*, 3506. [[CrossRef](#)]
22. Dupuis, J.; Fourmond, E.; Ballutaud, D.; Bererd, N.; Lemiti, M. Optical and structural properties of silicon oxynitride deposited by plasma enhanced chemical vapor deposition. *Thin Solid Film.* **2010**, *519*, 1325–1333. [[CrossRef](#)]
23. Ay, F.; Aydinli, A. Comparative investigation of hydrogen bonding in silicon based PECVD grown dielectrics for optical waveguides. *Opt. Mater.* **2004**, *26*, 33–46. [[CrossRef](#)]
24. Shams, Q.A.; Brown, W.D. Physical and Electrical Properties of Memory Quality PECVD Silicon Oxynitride. *J. Electrochem. Soc.* **1990**, *137*, 1244–1247. [[CrossRef](#)]
25. Shi, Y.; He, L.; Guang, F.; Li, L.; Xin, Z.; Liu, R. A review: Preparation, performance, and applications of silicon oxynitride film. *Micromachines* **2019**, *10*, 552. [[CrossRef](#)] [[PubMed](#)]
26. Wong, H.; Yang, B.L.; Cheng, Y.C. Chemistry of silicon oxide annealed in ammonia. *Appl. Surf. Sci.* **1993**, *72*, 49–54. [[CrossRef](#)]
27. Dumas, L.; Quesnel, E.; Robic, J.-Y.; Pauleau, Y. Characterization of magnesium fluoride thin films deposited by direct electron beam evaporation. *J. Vac. Sci. Technol. A Vac. Surf. Film.* **2000**, *18*, 465–469. [[CrossRef](#)]

28. Kinoshita, K.; Nishibori, M. Porosity of MgF_2 Films. Evaluation Based on Changes in Refractive Index Due To Adsorption of Vapors. *J. Vac. Sci. Technol.* **1969**, *6*, 730–733. [[CrossRef](#)]
29. Sealy, B.J.; Crocker, A.J.; Lee, M.J.; Egerton, R.F. Electrical properties of evaporated MgF_2 films. *Thin Solid Film.* **1972**, *11*, 365–376. [[CrossRef](#)]
30. Gao, R.; Lei, D.; He, Z.; Chen, Y.; Huang, Y.; En, Y.; Xu, X.; Zhang, F. Effect of Moisture Stress on the Resistance of HfO_2/TaO_x -Based 8-Layer 3D Vertical Resistive Random Access Memory. *IEEE Electron Device Lett.* **2020**, *41*, 38–41. [[CrossRef](#)]
31. Bagdzevicius, S.; Maas, K.; Boudard, M.; Burriel, M. Interface-type resistive switching in perovskite materials. *J. Electroceram.* **2017**, *39*, 157–184. [[CrossRef](#)]
32. Das, N.C.; Kim, M.; Kwak, D.U.; Rani, J.R.; Hong, S.M.; Jang, J.H. Effects of the Operating Ambiance and Active Layer Treatments on the Performance of Magnesium Fluoride Based Bipolar RRAM. *Nanomaterials* **2022**, *12*, 605. [[CrossRef](#)]
33. Santosh, K. Nanoscale Semiconductor Memories: Technology and Applications. In *Nanoscale Semiconductor Memories*; CRC Press: Boca Raton, FL, USA, 2017.
34. Zahoor, F.; Azni Zulkifli, T.Z.; Khanday, F.A. Resistive Random Access Memory (RRAM): An Overview of Materials, Switching Mechanism, Performance, Multilevel Cell (mlc) Storage, Modeling, and Applications. *Nanoscale Res. Lett.* **2020**, *15*, 90. [[CrossRef](#)]
35. Guo, T.; Sun, B.; Zhou, Y.; Zhao, H.; Lei, M.; Zhao, Y. Overwhelming coexistence of negative differential resistance effect and RRAM. *Phys. Chem. Chem. Phys.* **2018**, *20*, 20635–20640. [[CrossRef](#)]
36. Sun, H.; Liu, Q.; Long, S.; Lv, H.; Banerjee, W.; Liu, M. Multilevel unipolar resistive switching with negative differential resistance effect in $Ag/SiO_2/Pt$ device. *J. Appl. Phys.* **2014**, *116*, 154509. [[CrossRef](#)]
37. Wu, F.; Si, S.; Shi, T.; Zhao, X.; Liu, Q.; Liao, L.; Lv, H.; Long, S.; Liu, M. Negative differential resistance effect induced by metal ion implantation in SiO_2 film for multilevel RRAM application. *Nanotechnology* **2018**, *29*, 54001. [[CrossRef](#)] [[PubMed](#)]
38. Feng, Y.; Huang, P.; Zhou, Z.; Zhu, D.; Han, R.; Ding, X.; Liu, L.; Liu, X.; Kang, J. Ru-based Oxide Resistive Random Access Memory for BEOL-Compatible Novel NVM Applications. In Proceedings of the 2018 14th IEEE International Conference on Solid-State and Integrated Circuit Technology (ICSICT), Qingdao, China, 31 October–3 November 2018; p. 2628. [[CrossRef](#)]
39. Feng, Y.; Huang, P.; Zhou, Z.; Ding, X.; Liu, L.; Liu, X.; Kang, J. Negative Differential Resistance Effect in Ru-Based RRAM Device Fabricated by Atomic Layer Deposition. *Nanoscale Res. Lett.* **2019**, *14*, 2–6. [[CrossRef](#)] [[PubMed](#)]
40. Onofrio, N.; Guzman, D.; Strachan, A. Atomic origin of ultrafast resistance switching in nanoscale electrometallization cells. *Nat. Mater.* **2015**, *14*, 440–446. [[CrossRef](#)] [[PubMed](#)]
41. Jung, K.; Seo, H.; Kim, Y.; Im, H.; Hong, J.P.; Park, J.W.; Lee, J.K. Temperature dependence of high- and low-resistance bistable states in polycrystalline NiO films. *Appl. Phys. Lett.* **2007**, *90*, 052104. [[CrossRef](#)]
42. Uenuma, M.; Ishikawa, Y.; Uraoka, Y. Joule heating effect in nonpolar and bipolar resistive random access memory. *Appl. Phys. Lett.* **2015**, *107*, 073503. [[CrossRef](#)]
43. Chen, A.B. Size-Dependent Metal-Insulator Transition in Pt-Dispersed SiO_2 Thin Film: A Candidate for Future Nonvolatile Memory. Ph.D. Thesis, University of Pennsylvania, Philadelphia, PA, USA, 2011; p. 117.
44. Pérez, E.; Wenger, C.; Grossi, A.; Zambelli, C.; Olivo, P.; Roelofs, R. Impact of temperature on conduction mechanisms and switching parameters in HfO_2 -based 1T-1R resistive random access memories devices. *J. Vac. Sci. Technol. B Nanotechnol. Microelectron. Mater. Process. Meas. Phenom.* **2017**, *35*, 01A103. [[CrossRef](#)]
45. Chiu, F.C. A review on conduction mechanisms in dielectric films. *Adv. Mater. Sci. Eng.* **2014**, *2014*, 578168. [[CrossRef](#)]
46. Li, Y.T.; Long, S.B.; Liu, Q.; Lü, H.B.; Liu, S.; Liu, M. An overview of resistive random access memory devices. *Chin. Sci. Bull.* **2011**, *56*, 3072–3078. [[CrossRef](#)]
47. Lim, E.W.; Ismail, R. Conduction mechanism of valence change resistive switching memory: A survey. *Electronics* **2015**, *4*, 586–613. [[CrossRef](#)]
48. Chiu, F.C.; Chou, H.W.; Lee, J.Y.M. Electrical conduction mechanisms of metal La_2O_3/Si structure. *J. Appl. Phys.* **2005**, *97*, 103503. [[CrossRef](#)]
49. Rebib, F.; Tomasella, E.; Dubois, M.; Cellier, J.; Sauvage, T.; Jacquet, M. Structural and optical investigations of SiO_xNy thin films deposited by R.F. sputtering. *Surf. Coat. Technol.* **2005**, *200*, 330–333. [[CrossRef](#)]
50. Park, J.H.; Kim, H.D.; Hong, S.M.; Yun, M.J.; Jeon, D.S.; Kim, T.G. Improved resistive switching phenomena observed in $SiNx$ -based resistive switching memory through oxygen doping process. *Phys. Status Solidi-Rapid Res. Lett.* **2014**, *8*, 239–242. [[CrossRef](#)]